J|A|C|S
ARTICLES
Published on Web 03/03/2007

$XeOF_2$, $F_2OXeN{\equiv}CCH_3$, and $XeOF_2{\cdot}n$HF: Rare Examples of Xe(IV) Oxide Fluorides

David S. Brock, Vural Bilir, Hélène P. A. Mercier, and Gary J. Schrobilgen*

Contribution from the Department of Chemistry, McMaster University, Hamilton, Ontario, L8S 4M1, Canada

Received October 18, 2006; E-mail: schrobil@mcmaster.ca

Abstract: The syntheses of $XeOF_2$, $F_2OXeN{\equiv}CCH_3$, and $XeOF_2{\cdot}n$HF and their structural characterizations are described in this study. All three compounds are explosive at temperatures approaching 0 °C. Although $XeOF_2$ had been previously reported, it had not been isolated as a pure compound. Xenon oxide difluoride has now been characterized in CH_3CN solution by ^{19}F, ^{17}O, and ^{129}Xe NMR spectroscopy. The solid-state Raman spectra of $XeOF_2$, $F_2OXeN{\equiv}CCH_3$, and $XeOF_2{\cdot}n$HF have been assigned with the aid of $^{16}O/^{18}O$ and $^{1}H/^{2}H$ enrichment studies and electronic structure calculations. In the solid state, the structure of $XeOF_2$ is a weakly associated, planar monomer, ruling out previous speculation that it may possess a polymeric chain structure. The geometry of $XeOF_2$ is consistent with a trigonal bipyramidal, AX_2YE_2, VSEPR arrangement that gives rise to a T-shaped geometry in which the two free valence electron lone pairs and Xe−O bond domain occupy the trigonal plane and the Xe−F bond domains are trans to one another and perpendicular to the trigonal plane. Quantum mechanical calculations and the Raman spectra of $XeOF_2{\cdot}n$HF indicate that the structure likely contains a single HF molecule that is H-bonded to oxygen and also weakly F-coordinated to xenon. The low-temperature (−173 °C) X-ray crystal structure of $F_2OXeN{\equiv}CCH_3$ reveals a long Xe−N bond trans to the Xe−O bond and a geometrical arrangement about xenon in which the atoms directly bonded to xenon are coplanar and $CH_3C{\equiv}N$ acts as a fourth ligand in the equatorial plane. The two fluorine atoms are displaced away from the oxygen atom toward the Xe−N bond. The structure contains two sets of crystallographically distinct $F_2OXeN{\equiv}CCH_3$ molecules in which the bent Xe−N−C moiety lies either in or out of the $XeOF_2$ plane. The geometry about xenon is consistent with an AX_2YZE_2 VSEPR arrangement of bond pairs and electron lone pairs and represents a rare example of a Xe(IV)−N bond.

Introduction

Among the principal formal oxidation states of xenon, +2, +4, +6, and +8, the +4 oxidation state has been little studied and is presently limited to XeF_5^-,[1] XeF_4,[2−4] $Xe(OTeF_5)_4$,[3,5,6] $Xe(OTeF_5)_{4-x}F_x$ ($x = 0-3$),[3] several XeF_3^+ salts,[7−9] and $[C_6F_5XeF_2][BF_4]$,[10] and to preliminary reports of $F_3XeOIOF_4$,[11] $F_xXe(OTeF_5)_{3-x}^+$ ($x = 0-2$),[12] $XeOF_2$,[13−15] and $XeOF_3^-$.[15] The modest and slow progress that has been made in the syntheses and structural investigations of xenon(IV) oxide fluoride species contrasts with that of xenon(VI)[16,17] and stems from the explosive nature of the synthetic precursor, $XeOF_2$, and the need to find a reliable, high-yield synthesis for $XeOF_2$.

Although vibrational spectroscopic evidence for $XeOF_2$ has been communicated on three prior occasions, none of these studies resulted in the unambiguous characterization or the isolation of pure $XeOF_2$. In two studies, $XeOF_2$ was reported as the product of the co-condensation of H_2O and XeF_4 vapors at low temperatures. Co-deposited thin films were characterized by infrared spectroscopy,[13,14] yielding infrared spectra that were in good agreement with each other. In one of these studies, samples were also prepared by a bulk co-condensation procedure and characterized by Raman spectroscopy.[14] Both the bulk co-condensation product[14] and the infrared spectra obtained from thin films[13,14] are shown by the present work to be mixtures of $XeOF_2$ and $XeOF_2{\cdot}n$HF. One of the components in the latter studies, $XeOF_2{\cdot}n$HF, was subsequently synthesized as the sole

(1) Christe, K. O.; Dixon, D. A.; Curtis, E. C.; Mercier, H. P.; Sanders, J. C. P.; Schrobilgen, G. J. *J. Am. Chem. Soc.* **1991**, *113*, 3351−3361.
(2) Claassen, H. H.; Chernick, C. L.; Malm, J. G. *J. Am. Chem. Soc.* **1963**, *85*, 1927−1928.
(3) Schumacher, G. A.; Schrobilgen, G. J. *Inorg. Chem.* **1984**, *23*, 2923−2929.
(4) Levy, H. A.; Burns, J. H.; Agron, P. A. *Science* **1963**, *139*, 1208−1209.
(5) Jacob, E.; Lentz, D.; Seppelt, K.; Simon, A. *Z. Anorg. Allg. Chem.* **1981**, *472*, 7−25.
(6) Turowsky, L.; Seppelt, K. *Z. Anorg. Allg. Chem.* **1992**, *609*, 153−156.
(7) Gillespie, R. J.; Schrobilgen, G. J.; Landa, B. *Chem. Commun.* **1971**, 1543−1544.
(8) Boldrini, P.; Gillespie, R. J.; Ireland, P. R.; Schrobilgen, G. J. *Inorg. Chem.* **1974**, *13*, 1690−1694.
(9) McKee, D. E.; Zalkin, A.; Bartlett, N. *Inorg. Chem.* **1973**, *12*, 1713−1717.
(10) Frohn, H.-J.; Leblond, N; Lutar, K.; Žemva, B. *Angew. Chem., Int. Ed. Engl.* **2000**, *39*, 391−393.
(11) Syvret, R. G.; Schrobilgen, G. J. *J. Chem. Soc. Chem. Commun.* **1985**, 1529−1530.
(12) Syvret, R. G.; Mitchell, K. M.; Sanders, J. C. P.; Schrobilgen, G. J. *Inorg. Chem.* **1992**, *31*, 3381−3385.
(13) Ogden, J. S.; Turner, J. J. *Chem. Comm.* **1966**, *19*, 693−694.
(14) Jacob, E.; Opferkuch, R. *Angew. Chem., Int. Ed. Engl.* **1976**, *15*, 158−159.
(15) Gillespie, R. J.; Schrobilgen, G. J. *Chem. Commun.* **1977**, 595−597.
(16) Holloway, J. H.; Hope, E. G. *Adv. Inorg. Chem.* **1998**, *46*, 51−100.
(17) Whalen, J. M.; Schrobilgen, G. J. *Helium-Group Gases Compounds*, 4 ed.; John Wiley & Sons, Inc.: New York, 1994; Vol. 13, pp 38−53.

10.1021/ja0673480 CCC: $37.00

product by the hydrolysis of finely divided XeF_4 in HF but was erroneously attributed to $XeOF_2$.[15]

The inconsistencies related to the vibrational spectra of the reaction products of XeF_4 and H_2O in the prior published work, the lack of corroborating structural evidence for the products obtained in these early studies, and the absence of a facile synthesis of synthetically useful amounts of pure $XeOF_2$ motivated the present study, which describes reproducible high-yield and high-purity routes to $XeOF_2$, $F_2OXeN{\equiv}CCH_3$, and $XeOF_2{\cdot}n$HF and their structure determinations, offering the potential to extend the range of oxo-derivatives of xenon(IV).

Results and Discussion

Syntheses and Properties of $XeOF_2$, $F_2OXeN{\equiv}CCH_3$, and $XeOF_2{\cdot}n$HF. Reaction progress and the purities of all products were routinely monitored by recording the low-temperature Raman spectra (−150 °C) of the solids which were isolated as their natural abundance, ^{18}O-enriched (98.6 atom %), and ^{2}H-enriched (99.5 atom %) isotopomers.

Xenon oxide difluoride was initially obtained as the CH_3CN adduct by low-temperature hydrolysis of XeF_4 in CH_3CN solution containing 2.00 M H_2O according to eq 1. Water was

$$XeF_4 + H_2O + CH_3CN \xrightarrow[-45\ \text{to}\ -42\ ^\circ\text{C}]{CH_3CN} F_2OXeN{\equiv}CCH_3 + 2HF \quad (1)$$

added in ca. 3−5% stoichiometric excess to avoid unreacted XeF_4 contaminant in the product. A 2-fold stoichiometric excess of H_2O yielded only $XeOF_2$ and did not result in the formation of other xenon-containing products such as OXe(OH)F, OXe(OH)$_2$, or XeO_2. Although HF resulting from the hydrolysis of XeF_4 forms an adduct with CH_3CN (see Raman Spectroscopy), it could be removed under dynamic vacuum along with the solvent at −45 to −42 °C. The $F_2OXeN{\equiv}CCH_3$ adduct crystallized as pale yellow blades at −35 to −45 °C which were isolated by removal of the bulk solvent under dynamic vacuum at −45 to −42 °C while periodically monitoring its removal by low-temperature Raman spectroscopy.

Further pumping on polycrystalline $F_2OXeN{\equiv}CCH_3$ for several hours at −45 to −42 °C, resulted in slow removal of adducted CH_3CN (eq 2), with the time depending on the sample size, leaving behind $XeOF_2$ as a bright-yellow amorphous powder. Neither $F_2OXeN{\equiv}CCH_3$ nor $XeOF_2$ were soluble in SO_2ClF up to −78 °C and were recovered unchanged upon removal of SO_2ClF under vacuum at −78 °C.

$$F_2OXeN{\equiv}CCH_3 \xrightarrow[-45\ \text{to}\ -42\ ^\circ\text{C}]{\text{dynamic vac.}} XeOF_2 + CH_3CN \quad (2)$$

Addition of anhydrous HF to $XeOF_2$ at −78 °C resulted in a very pale yellow and insoluble powder having a new Raman spectrum in which several bands were sensitive to $^{1/2}H$ isotopic substitution (see Raman Spectroscopy). The results indicated that $XeOF_2{\cdot}n$HF was formed according to eq 3. When $XeOF_2{\cdot}n$HF was pumped under dynamic vacuum at −78 °C,

$$XeOF_{2(s)} + n\text{HF} \xrightarrow[12\ \text{h@}-78\ ^\circ\text{C}]{\text{HF}} XeOF_2{\cdot}n\text{HF} \quad (3)$$

with frequent agitation, bound HF was slowly removed over a period of several hours, regenerating unsolvated $XeOF_2$.

All three compounds, $F_2OXeN{\equiv}CCH_3$, $XeOF_2$, and $XeOF_2{\cdot}n$HF, are kinetically stable at −78 °C for indefinite periods of time, but decompose rapidly to explosively with emission of blue light upon warming to 0 °C. The major gas-phase decomposition pathway is O_2 elimination according to eq 4 whereas the minor pathway is disproportionation to

$$XeOF_{2(g)} \rightarrow XeF_{2(g)} + {}^1/_2O_{2(g)} \quad (4)$$

$$\Delta H^\circ_{rxn} = -245.8\ \text{kJ mol}^{-1}$$

$$\Delta G^\circ_{rxn} = -259.3\ \text{kJ mol}^{-1}$$

MP2/(SDB-)cc-pVTZ

Xe(II) and Xe(VI) according to eq 5. Both decomposition pathways have been observed in CH_3CN solutions of $XeOF_2$

$$2XeOF_{2(g)} \rightarrow XeF_{2(g)} + XeO_2F_{2(g)} \quad (5)$$

$$\Delta H^\circ_{rxn} = -98.8\ \text{kJ mol}^{-1}$$

$$\Delta G^\circ_{rxn} = -86.9\ \text{kJ mol}^{-1}$$

MP2/(SDB-)cc-pVTZ

and inferred from the formation of small, but unequal, molar amounts of XeF_2 and XeO_2F_2 (see NMR Spectroscopy).

^{129}Xe, ^{19}F, and ^{17}O NMR Spectroscopy. In contrast with HF, $XeOF_2$ has appreciable solubility in CH_3CN, allowing the low temperature (−42 °C) ^{19}F, ^{17}O, and ^{129}Xe NMR spectra to be recorded.

The ^{19}F NMR spectrum of a solution of $XeOF_2$ prepared by the hydrolysis of XeF_4 in CH_3CN consisted of a singlet (−48.8 ppm) with accompanying ^{129}Xe (I = 1/2, 26.44%) satellites corresponding to $^1J(^{19}F-^{129}Xe)$ = 3446 Hz (Figure 1a). In addition, a weak singlet (−179.2 ppm) corresponding to XeF_2 (~2% or less) with accompanying ^{129}Xe (I = 1/2, 26.44%) satellites ($^1J(^{129}Xe-^{19}F)$ = 5641 Hz), a second weaker singlet (83.2 ppm) corresponding to XeO_2F_2 (~1% or less) with accompanying ^{129}Xe satellites ($^1J(^{129}Xe-^{19}F)$ = 1320 Hz), and an intense singlet corresponding to HF ($\delta(^{19}F)$, −179.8 ppm,[18] $\Delta\nu_{1/2}$ = 83 Hz) were observed. The ^{129}Xe NMR spectrum of $XeOF_2$ consisted of a triplet ($\delta(^{129}Xe)$, 242.3 ppm) arising from $^1J(^{129}Xe-^{19}F)$ = 3447 Hz (Figure 1c). Weak XeF_2 [$\delta(^{129}Xe)$, −1779.0 ppm, $^1J(^{19}F-^{129}Xe)$ = 5648 Hz] and XeO_2F_2 [$\delta(^{129}Xe)$, 227.4 ppm, $^1J(^{19}F-^{129}Xe)$ = 1324 Hz] resonances were also visible as triplets in the ^{129}Xe NMR spectrum. In several preparations, small amounts (ca. 0.01%) of unreacted XeF_4 [$\delta(^{19}F)$, −20.5 ppm; $\delta(^{129}Xe)$, 336.7 ppm; $^1J(^{129}Xe-^{19}F)$ = 3911 Hz] were also observed. The increased shielding (lower frequency) of the ^{129}Xe resonance of $XeOF_2$ relative to that of XeF_4 is opposite to the decreased shielding (high-frequency shift) that occurs upon increasing oxygen substitution observed for Xe(VI): XeF_6, $XeOF_4$, XeO_2F_2, XeO_3 and for Xe(VIII): XeO_3F_2, XeO_4.[19] The trend reversal may arise because one or

(18) Fujiwara, F. Y.; Martin, J. S. *J. Am. Chem. Soc.* **1974**, *96*, 7625−7631. This reference established that HF is molecular in CH_3CN solvent; $\delta(^{19}F)$ = −181.1 ppm and $^1J(^{19}F-^1H)$ = 476 Hz at -40 °C. In the present work, $^1J(^{19}F-^1H)$ was collapsed to a broad line which is presumably the result of exchange with residual H_3O^+ (vide infra).

(19) Gerken, M.; Schrobilgen, G. J. *Coord. Chem. Rev.* **2000**, *197*, 335−395.

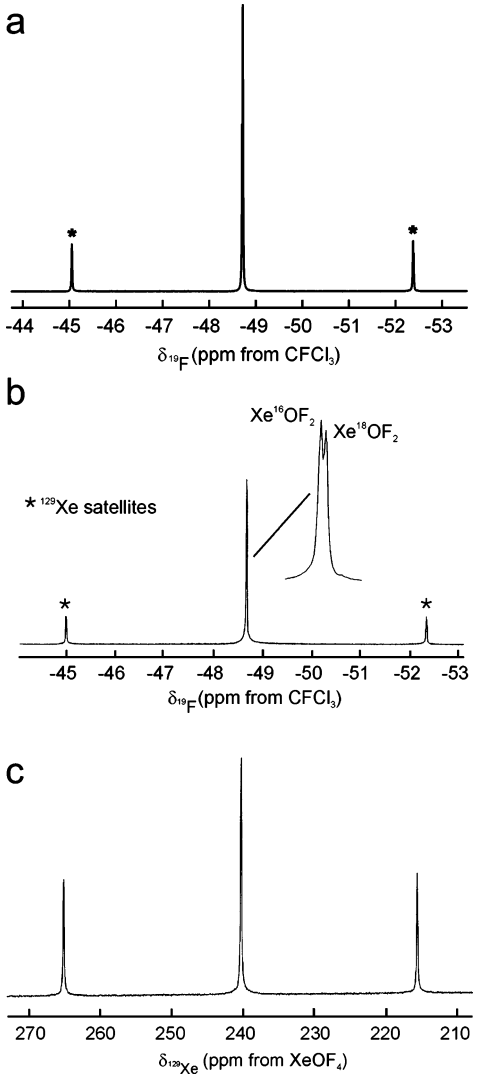

Figure 1. The ^{19}F NMR spectrum (470.599 MHz) of (a) $Xe^{16}OF_2$ and (b) $Xe^{16,18}OF_2$, and (c) the ^{129}Xe NMR spectrum (138.339 MHz) of $Xe^{16}OF_2$. Spectra were recorded in CH_3CN at −45 °C.

more CH_3CN molecules are nitrogen coordinated to the Lewis acidic xenon center of $XeOF_2$ (see X-ray Crystal Structure of $F_2OXeN{\equiv}CCH_3$), contributing added shielding to ^{129}Xe and ^{19}F. Upon donation of nitrogen electron lone pair density into the xenon valence shell, the ^{129}Xe nuclear shielding is enhanced and the effective electronegativity of Xe(IV) is decreased, resulting in increased ^{19}F shielding relative to that of XeF_4. Failure to observe separate resonances for bound and free CH_3CN in the low-temperature ^1H and ^{14}N NMR spectra of $XeOF_2$ solutions in CH_3CN indicates that the Xe−N donor−acceptor interaction(s) is (are) labile under these conditions.

A solution of $XeOF_2$ in CH_3CN was also prepared by the reaction of XeF_4 with ^{17}O-enriched water (35.4%, ^{16}O; 21.9%, ^{17}O; 42.77%, ^{18}O) dissolved in CH_3CN at −45 °C. The central line and ^{129}Xe satellites of the ^{19}F resonance [$\delta(^{19}F)$, −48.6 ppm; $^1J(^{129}Xe-^{19}F) = 3448$ Hz] were split as a result of the secondary isotope shift [$^2\Delta^{19}F(^{18/16}O) = -0.0136$ ppm] between $Xe^{16}OF_2$ and $Xe^{18}OF_2$ (Figure 1b). The observation of the isotope shift confirms the assignment of the singlet and its satellites to $XeOF_2$ and represents the only two-bond isotope shift that has been observed for a xenon compound. The ^{17}O NMR spectrum showed an intense broad resonance at $\delta(^{17}O) = 209$ ppm ($\Delta\nu_{1/2} = 1300$ Hz), assigned to $XeOF_2$, but was too broad, owing to quadrupolar relaxation, to show $^2J(^{19}F-^{17}O)$ coupling or ^{129}Xe satellites arising from $^1J(^{129}Xe-^{17}O)$ coupling. These couplings also were not visible in the ^{129}Xe [$\delta = 240.1$ ppm; $^1J(^{129}Xe-^{19}F) = 3448$ Hz] and the ^{19}F NMR spectra because quadrupolar relaxation by the ^{17}O, and its attendant broadening, made it impossible to distinguish the equi-intense components of the anticipated sextets ($I = {}^5/_2$) from the spectral baselines. A weak, broad resonance at $\delta(^{17}O) = 3.4$ ppm, which likely arises from excess H_3O^+, and a weak, but very sharp resonance at $\delta(^{17}O) = 77.7$ ppm ($\Delta\nu_{1/2} \approx 10$ Hz) were also observed in the ^{17}O NMR spectrum. The latter resonance likely results from the decomposition of $XeOF_2$ in CH_3CN at −45 °C. Although $XeOF_2$ was shown to decompose according to eq 6 in CH_3CN solvent, it may also act as a source of atomic oxygen (eq 7)

$$XeOF_2 \xrightarrow[-45\ ^\circ C]{CH_3CN} XeF_2 + {}^1/_2O_2 \quad (6)$$

$$XeOF_2 \xrightarrow[-45\ ^\circ C]{CH_3CN} XeF_2 + [O] \quad (7)$$

$$CH_3C{\equiv}N + [O] \xrightarrow[-45\ ^\circ C]{CH_3CN} CH_3C{\equiv}N^+-O^- \quad (8)$$

which is expected to react with CH_3CN to give acetonitrile *N*-oxide according to eq 8. The reaction of CH_3CN with atomic oxygen, $O(^3P)$, generated by laser flash photolysis of pyridine *N*-oxide in CH_3CN solvent, has been previously documented.[20,21] The narrow ^{17}O line width is consistent with the axial symmetry of $CH_3C{\equiv}N^+-O^-$.

Table 1. Summary of Crystal Data and Refinement Results for $F_2OXeN{\equiv}CCH_3$

space group	$P2_1/c$ (No. 14)
a (Å)	8.7819(4)
b (Å)	13.9862(6)
c (Å)	11.0182(6)
β (deg.)	128.476(2)
V (Å^3)	1059.47(1)
Z (molecules/unit cell)	8
mol. wt. (g mol^{-1})	1810.83
ρ_{calc} (g cm^{-3})	2.838
T (°C)	−173
μ (mm^{-1})	6.43
λ (Å)	0.71073
final agreement factors[a]	$R_1 = 0.0299$ $wR_2 = 0.0675$

[a] R_1 is defined as $= \Sigma||F_o| - |F_c||/\Sigma|F_o|$ for $I > 2\sigma(I)$; wR_2 is defined as $[\Sigma[w(F_o^2)^2 - F_c^2)^2]/\Sigma w(F_o^2)^2]^{1/2}$ for $I > 2\sigma(I)$.

X-ray Crystal Structure of $F_2OXeN{\equiv}CCH_3$. A summary of the refinement results and other crystallographic information are given in Table 1. Important bond lengths, bond angles, and contacts are listed in Table 2.

The structure of $F_2OXeN{\equiv}CCH_3$ consists of $XeOF_2$ molecules and CH_3CN ligands that interact by means of short Xe···N contacts (Figures 2 and 3). Two crystallographically independent adduct conformations define the asymmetric unit in which four molecules of each conformer comprise the contents of the unit cell. The Xe−N−C angles are bent in both conformers with the CH_3CN ligand lying in the $XeOF_2$ plane for one conformer and out of the $XeOF_2$ plane for the other conformer.

(20) Bucher, G.; Scaiano, J. C. *J. Phys. Chem.* **1994**, *98*, 12471−12473.
(21) Pasinszki, T.; Westwood, N. P. C. *J. Phys. Chem. A* **2001**, *105*, 1244−1253.

Table 2. Experimental and Calculated (C_1) Geometrical Parameters for $F_2OXeN{\equiv}CCH_3$

exptl[a]				SVWN[b]	MP2[b]
bond lengths (Å)					
bent in-plane structure[a]		bent out-of-plane structure[a]			
Xe(1)−O(1)	1.778(4)	Xe(2)−O(2)	1.782(4)	Xe(1)−O(1)	1.813	1.774
Xe(1)−F(1)	1.958(3)	Xe(2)−F(3)	1.975(3)	Xe(1)−F(1)	2.013	1.993
Xe(1)−F(2)	1.952(3)	Xe(2)−F(4)	1.981(3)	Xe(1)−F(2)	2.013	1.993
Xe(1)···N(1)	2.808(5)	Xe(2)···N(2)	2.752(5)	Xe(1)···N(1)	2.702	2.883
N(1)−C(10)	1.142(7)	N(2)−C(20)	1.127(7)	N(1)−C(1)	1.152	1.167
C(10)−C(11)	1.448(8)	C(20)−C(21)	1.453(8)	C(1)−C(2)	1.428	1.455
				C(2)−H	1.099	1.087
		bond angles (deg)				
F(1)−Xe(1)−F(2)	174.2(2)	F(3)−Xe(2)−F(4)	171.9(1)	F(1)−Xe(1)−F(2)	167.6	168.9
F(1)−Xe(1)−O(1)	92.4(2)	F(3)−Xe(2)−O(2)	94.1(2)	F(1)−Xe(1)−O(1)	96.2	95.6
F(2)−Xe(1)−O(1)	93.4(2)	F(4)−Xe(2)−O(2)	94.0(2)	F(2)−Xe(1)−O(1)	96.2	95.6
F(1)−Xe(1)···N(1)	90.1(2)	F(3)−Xe(2)···N(2)	84.5(1)	F(1)−Xe(1)···N(1)	83.7	84.4
F(2)−Xe(1)···N(1)	84.1(2)	F(4)−Xe(2)···N(2)	87.3(1)	F(2)−Xe(1)···N(1)	83.8	84.4
Xe(1)···N(1)−C(10)	164.9(4)	Xe(2)···N(2)−C(20)	134.6(4)	Xe(1)···N(1)−C(1)	179.2	179.4
N(1)−C(10)−C(11)	178.9(6)	N(2)−C(20)−C(21)	178.4(6)	N(1)−C(1)−C(2)	179.9	179.9
		long contacts (Å)				
		Xe(2)···N(1)	3.635(5)			
		Xe(2)···N(1A)	3.526(5)			

[a] Bent in-plane and out-of-plane structures and their labeling schemes are given in Figure 3. [b] (SDB-)cc-pVTZ basis set. The labeling scheme corresponds to that used in Figure 5b.

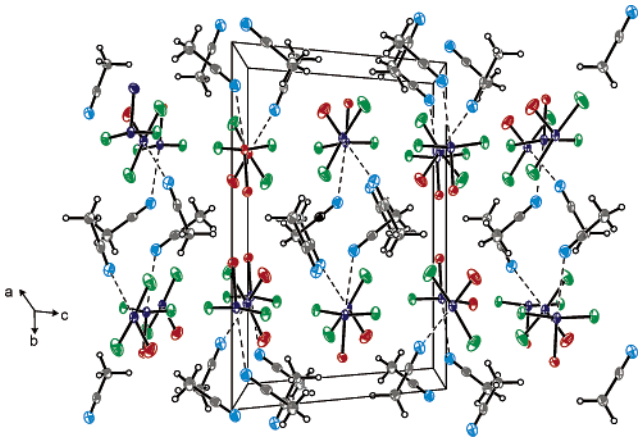

Figure 2. Crystal packing for $F_2OXeN{\equiv}CCH_3$ viewed along the *a*-axis; thermal ellipsoids are shown at the 50% probability level.

The primary coordination of the $XeOF_2$ moiety is a planar, T-shaped arrangement of two valence electron lone pairs and an oxygen double bond domain in the equatorial plane and two mutually *trans*-fluorine atoms perpendicular to that plane. The nitrogen electron pair donor atom of CH_3CN is coordinated trans to the oxygen atom and is coplanar with the $XeOF_2$ moiety in both conformers so that the geometry of the F_2OXeN moiety is consistent with an AX_2YZE_2 VSEPR[22] arrangement of three single bond domains (X and Z), one double bond domain (Y), and two electron lone pair domains (E), placing the valence electron lone pairs trans to one another.

The Xe−O bond lengths of both conformers are equal, within $\pm 3\sigma$ (1.778(4), 1.782(4) Å), and are somewhat longer than those observed in the neutral Xe(VI) and Xe(VIII) oxides and oxide fluorides $XeOF_4$ (1.713(3) Å),[23] XeO_2F_2 (1.714(4),[24] 1.734(9)[25] Å), XeO_3 (1.74(3)−1.77(3) Å),[26] and XeO_4 (1.736(2) Å).[27] Overall, the Xe−F bond lengths of $F_2OXeN{\equiv}CCH_3$ are comparable to those in XeF_4 (1.953(2) Å).[4] The Xe−F bond lengths of the out-of-plane conformer (1.975(3), 1.981(3) Å) are slightly longer when compared with those of the in-plane conformer (1.952(3), 1.958(3) Å), where the longer Xe−F bond lengths correspond to the shorter Xe−N bond in the out-of-plane conformer. The equatorial F−Xe−F angles (171.9(1)°, out-of-plane; 174.2(2)°, in-plane) are slightly bent away from the Xe−O double bond domain toward the Xe−N bond, in accord with the greater steric requirement of the double bond domain relative to that of a single bond domain. This angle is reproduced in the calculated structure (see Computational Results).

The in-plane conformer (Figure 3a) has a Xe(1)−N(1) distance of 2.808(5) Å and a Xe(1)−N(1)−C(10) angle of 164.9(4)°. The xenon atom of this conformer has no additional long contacts that are at, or less than, the sum of the van der Waals radii of Xe and F (3.63 Å)[28] or Xe and N (3.71 Å).[28] In the case of the out-of-plane conformer (Figure 3a), the nitrogen atom lies out of the $XeOF_2$ plane by 0.23 Å. The NCC moiety is rotated 57.8° out of the $XeOF_2$ plane and subtends an angle of 11.1° with the OXeN-axis. This conformer has a slightly shorter Xe(2)−N(2) distance (2.752(5) Å) and a smaller Xe(2)−N(2)−C(20) angle (134.6(4)°) than the in-plane conformer. The xenon atom of this conformer has two additional longer Xe(2)···N contacts, 3.526(5) [Xe(2)···N(1A)] and 3.635(5) [Xe(2)···N(1)] Å (Figure 3b), which are close to the sum of the Xe and N van der Waals radii and occur on opposite sides of the F_2OXeN-plane with dihedral angles of 63.6° and 117.4°, respectively. The shorter Xe(IV)−N distances in the present adducts are significantly less than the sum of the Xe and N van der Waals radii (3.71 Å),[28] but are significantly longer than all known Xe(II)−N bond lengths, namely,

(22) Gillespie, R. J.; Hargittai, I. In *The VSEPR Model of Molecular Geometry*; Allyn and Bacon: Boston, MA, 1991; pp 154−155.
(23) Pointner, B. E.; Suontamo, R. J.; Schrobilgen, G. J. *Inorg. Chem.* **2006**, *45*, 1517−1534.
(24) Peterson, S. W.; Willett, R. D.; Huston, J. L. *J. Chem. Phys.* **1973**, *59*, 453−459.
(25) Schrobilgen, G. J.; LeBlond, N.; Dixon, D. A. *Inorg. Chem.* **2000**, *39*, 2473−2487.
(26) Templeton, D. H.; Zalkin, A.; Forrester, J. D.; Williamson, S. M. *J. Am. Chem. Soc.* **1963**, *85*, 817.
(27) Gunderson, G.; Hedberg, K.; Huston, J. L. *J. Chem. Phys.* **1970**, *52*, 812−815.
(28) Bondi, A. *J. Phys. Chem.* **1964**, *68*, 441−451.

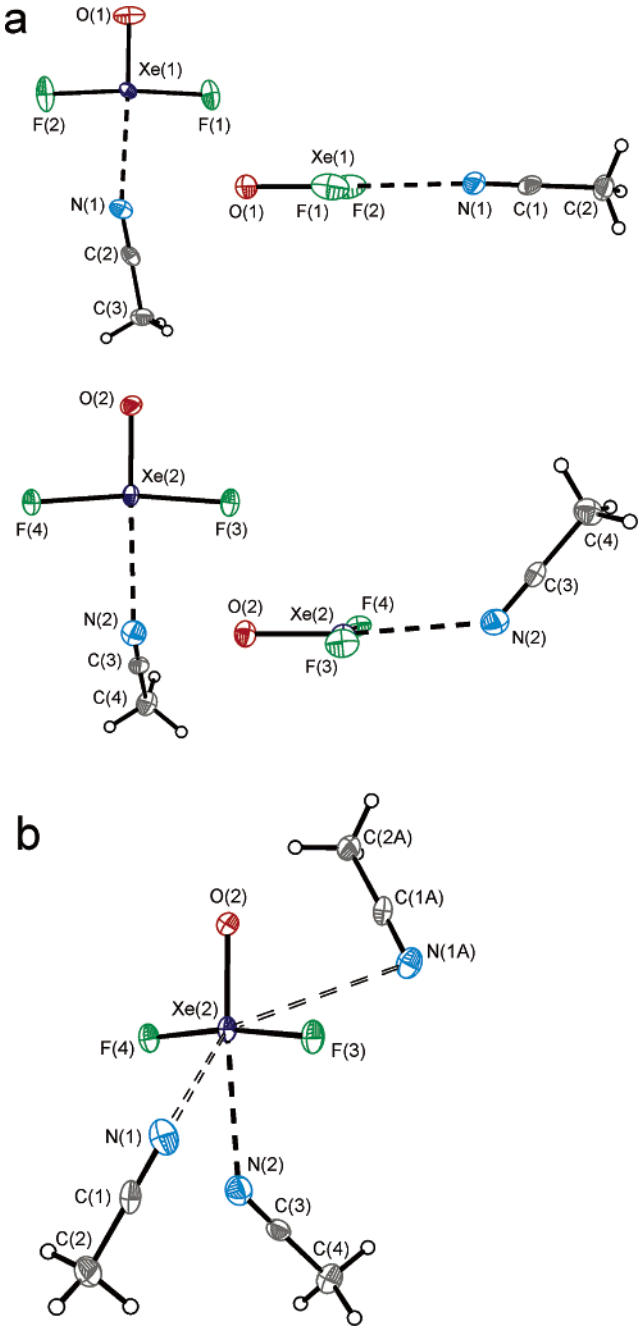

Figure 3. The X-ray crystal structure of $F_2OXeN{\equiv}CCH_3$ showing (a) two independent structural units and (b) the long contacts to Xe(2); thermal ellipsoids are shown at the 50% probability level.

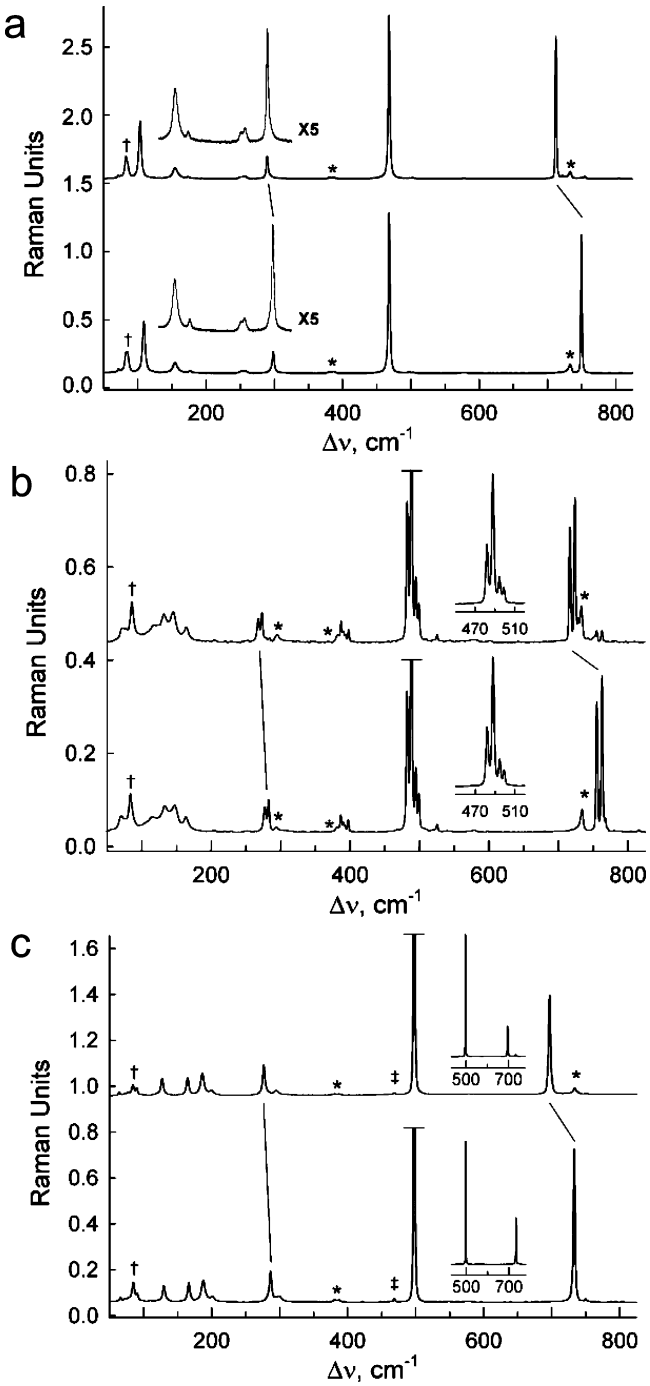

Figure 4. Raman spectra recorded at −150 °C using 1064-nm excitation for natural abundance (lower trace) and 98.6%. ^{18}O-enriched (upper trace): (a) $XeOF_2$, (b) $F_2OXeN{\equiv}CCH_3$, and (c) $XeOF_2{\cdot}n$HF. Symbols denote FEP sample tube lines (∗), instrumental artifact (†), and $XeOF_2$ (‡).

$[Xe(N(SO_2F)_2][Sb_3F_{16}]$ (2.02(1) Å),[29] $[F_5TeN(H)Xe][AsF_6]$ (2.044(4) Å),[30] $FXeN(SO_2F)_2$ (2.200(3) Å),[31] $[F_3S{\equiv}NXeF][AsF_6]$ (2.236(4) Å),[32] and $[C_6F_5XeN{\equiv}CCH_3][AsF_6]{\cdot}CH_3CN$ (2.681(8) Å).[33] Although the primary coordination of Xe(IV) in $XeOF_2$ is unsaturated and is expected to exhibit significant Lewis acidity, the Xe(IV)−N bond of $F_2OXeN{\equiv}CCH_3$ is significantly longer and weaker than the Xe(II)−N bonds of $F_3S{\equiv}NXeF^+$ and $C_6F_5XeN{\equiv}CCH_3^+$.

Raman Spectroscopy. The low-temperature Raman spectra of solid $Xe^{16/18}OF_2$, $F_2{}^{16/18}OXeN{\equiv}CCH_3$, and $Xe^{16/18}OF_2{\cdot}n$HF are shown in Figure 4. The observed and calculated frequencies and their assignments are listed in Tables 3−5 and S1. The modes associated with coordinated CH_3CN in $F_2{}^{16/18}OXeN{\equiv}CCH_3$ differ slightly from those of the free ligand, but could be easily identified (Tables 4 and S1−S3)

The spectral assignments for $Xe^{16/18}OF_2$, $F_2{}^{16/18}OXeN{\equiv}CCH_3$, and $Xe^{16/18}OF_2{\cdot}n^{1/2}$HF were made by comparison with the

(29) Faggiani, R.; Kennepohl, D. K.; Lock, C. J. L.; Schrobilgen, G. J. *Inorg. Chem.* **1986**, *25*, 563−571.
(30) Fir, B. A.; Whalen, J. M.; Mercier, H. P. A.; Dixon, D. A.; Schrobilgen, G. J. *Inorg. Chem.* **2006**, *45*, 1978−1996.
(31) Sawyer, J. F.; Schrobilgen, G. J.; Sutherland, S. J. *Inorg. Chem.* **1982**, *21*, 4064−4072.
(32) Smith, G. L.; Mercier, H. P. A.; Schrobilgen, G. J. *Inorg. Chem.* **2007**, *46*, 1369−1378.
(33) Frohn, H.-J.; Jakobs, S.; Henkel, G. *Angew. Chem., Int. Ed. Engl.* **1989**, *28*, 1506−1507.

Table 3. Experimental and Calculated Vibrational Frequencies[a] for $Xe^{16/18}OF_2$

exptl[b]		calcd[c]				assgnts[f]
		SVWN[d]		MP2[e]		
$Xe^{16}OF_2$	$Xe^{18}OF_2$	$Xe^{16}OF_2$	$Xe^{18}OF_2$	$Xe^{16}OF_2$	$Xe^{18}OF_2$	(C_{2v}) symmetry
749.9(83)	712.8(84)	795.4(16)[22]	756.2(14)[21]	939.1(9)[60]	892.5(9)[55]	ν(XeO)
n.o.	n.o.	572.3(<<1)[213]	573.8(<<1)[214]	582.5(<<1)[252]	583.8(<1)[253]	$\nu_{as}(XeF_2)$
467.8(100)	467.8(100)	505.3(25)[7]	505.3(25)[7]	509.1(37)[7]	508.9(37)[7]	$\nu_s(XeF_2)$
298.1(13)	289.0(14)	244.4(4)[3]	235.1(4)[3]	283.0(4)[3]	272.1(4)[3]	$\rho_{rock}(XeOF_2)$ ip
256.2(2)	256.2(2)	200.0(<<1)[21]	200.3(<<1)[20]	217.7(<<1)[25]	218.1(<<1)[25]	$\delta(XeF_2)$ oop
251.4(1)	251.8(1)					
175.7(1)	172.8(1)	154.9(<1)[14]	154.9(<1)[14]	176.1(<1)[19]	176.1(<1)[19]	$\delta(XeF_2)$ ip
154.0(6)	153.5(7)					
108.2(32)	102.4(35)					lattice mode

[a] Frequencies are given in cm^{-1}. The abbreviation denotes not observed (n.o.). [b] Raman spectrum of $Xe^{16/18}OF_2$ was recorded in an FEP sample tube at −150 °C using 1064-nm excitation. Values in parentheses are relative Raman intensities. [c] Values in parentheses are Raman intensities ($Å^4$ amu^{-1}), and values in square brackets denote infrared intensities (km mol^{-1}). [d] SVWN/(SDB-)cc-pVTZ. [e] MP2/(SDB-)cc-pVTZ. [f] Abbreviations denote symmetric (s), asymmetric (as), stretch (ν), bend (δ), rock (ρ_{rock}), in-plane (ip), and out-of-plane (oop). The in-plane and out-of-plane mode descriptions are relative to the $XeOF_2$ plane.

Table 4. Experimental and Calculated Vibrational Frequencies[a] for $F_2{}^{16/18}OXeN{\equiv}CCH_3$

exptl[b]		calcd[c]				assgnts[f]
		SVWN[d]		MP2[e]		
$F_2{}^{16}OXeNCCH_3$	$F_2{}^{18}OXeNCCH_3$	$F_2{}^{16}OXeNCCH_3$	$F_2{}^{18}OXeNCCH_3$	$F_2{}^{16}OXeNCCH_3$	$F_2{}^{18}OXeNCCH_3$	(C_1) symmetry
3009.1(10)	3008.7(10)	3067.6(78)[4]	3067.6(78)[4]	3198.7(60)[<1]	3198.7(60)[<1]	$\nu_{as}(CH_3)$
2999.0(10)	2999.0(11)	3066.7(79)[4]	3066.6(79)[4]	3198.2(60)[<1]	3198.2(60)[<1]	
2937.8(59)	2937.8(60)	2983.7(266)[3]	2983.6(266)[3]	3101.9(185)[<<1]	3101.9(185)[<<1]	$\nu_s(CH_3)$
2726.1(1)	2726.1(1)					*g*
2297.1(2)	2297.1(2)					*h*
2287.0(7)	2287.0(6)					
2253.7(51)	2254.1(51)	2347.2(287)[68]	2347.5(286)[67]	2234.7(96)[8]	2234.7(96)[8]	ν(CN)
1437.4(1), br	1436.0(2), br	1383.5(9)[15]	1383.5(9)[15]	1491.1(7)[11]	1491.1(7)[11]	$\delta_{as}(CH_3)$
1406.6(1), br	1409.9(1), br	1383.4(9)[15]	1383.4(9)[15]	1491.1(7)[11]	1491.1(7)[11]	
1370.4(5)	1370.4(6)	1333.5(14)[8]	1333.4(14)[8]	1416.6(4)[1]	1416.6(4)[1]	$\delta_s(CH_3)$
1356.9(6)	1357.1(6)					
1034.3(1)	1034.0(1)	995.7(<1)[7]	995.7(<1)[7]	1065.5(<1)[2]	1065.5(<1)[2]	$\rho_{rock}(CH_3)$
		995.6(<1)[7]	995.7(<1)[7]	1065.4(<<1)[2]	1065.4(<1)[2]	
926.3(5)	925.9(5)					
924.0(9)	924.0(8)	974.1(15)[5]	973.7(15)[5]	942.7(10)[6]	942.7(10)[7]	ν(CC)
766.8(5)	728.6(8)					
762.4(51)	724.1(47)	795.9(54)[64]	756.7(49)[61]	938.4(19)[100]	892.0(17)[92]	ν(XeO)
754.7(43)	717.1(38)					
525.2(2)	525.0(2)	549.0(<<1)[214]	550.4(<<1)[214]	565.0(<<1)[250]	566.5(<<1)[251]	$\nu_{as}(XeF_2)$
499.1(12)	498.7(13)					
494.4(21)	494.5(21)					
488.1(100)	488.1(100)	486.3(24)[3]	486.3(24)[3]	493.1(37)[5]	493.1(37)[5]	$\nu_s(XeF_2)$
481.8(46)	481.8(46)					
397.4(4)	397.2(4)	387.0(2)[1]	386.7(2)[<1]	374.0(2)[1]	374.0(2)[1]	δ(CCN)
392.6(2)	392.6(3)	384.8(2)[~0]	384.7(2)[~0]	372.6(2)[<1]	372.6(2)[<1]	
390.2(3)	389.7(4)					
283.2(11)	272.3(10)	242.7(4)[20]	233.3(3)[2]	282.0(4)[3]	271.2(4)[2]	$\rho_{rock}(XeOF_2)$ ip
277.4(8)	267.0(8)					
n.o.	n.o.	215.5(<1)[26]	214.9(<1)[26]	226.9(<1)[29]	226.8(<1)[28]	$\delta(OXeF_2N)$ oop
164.1(5)	162.9(5)	177.7(~0)[28]	177.6(~0)[28]	187.7(<1)[30]	187.9(<1)[30]	ν(XeN) + $\delta(XeF_2)$ ip
147.9(9)	144.3(10)					
133.7(9)	130.4(9)	119.6(2)[<1]	119.4(2)[~0]	101.1(1)[1]	101.1(1)[1]	ν(XeN) − $\delta(XeF_2)$ ip
116.4(5)	117.1(6)					
		108.8(2)[2]	106.7(2)[2]	97.2(2)[5]	95.0(2)[5]	δ(OXeN) ip + minor $\delta(XeF_2)$ oop
		83.6(<<1)[4]	83.9(<1)[4]	81.4(<1)[4]	81.3(<1)[4]	δ(XeNC) ip
		(31.0)(<<1)[2]	30.5(<<1)[2]	34.4(<<1)[1]	33.7(⟨⟨1)[1]	coupled deformations
		14.9(<1)[~0]	21.3(<<1)[<1]	16.6(2)[1]	16.4(2)[1]	
		6.0(2)[2]	7.9(2)[2]	8.9(<<1)[<<1]	8.9(<<1)[<<1]	

[a] Frequencies are given in cm^{-1}. The abbreviations denote broad (br) and not observed (n.o.). Additional abbreviations are given in footnote f of Table 3. [b] Raman spectrum of $F_2{}^{16/18}OXeN{\equiv}CCH_3$ was recorded in an FEP sample tube at −150 °C using 1064-nm excitation. Values in parentheses are relative Raman intensities. [c] Values in parentheses are Raman intensities ($Å^4$ amu^{-1}), and values in square brackets are infrared intensities (km mol^{-1}). [d] SVWN/(SDB-)cc-pVTZ. [e] MP2/(SDB-)cc-pVTZ. [f] Bond elongations and angle openings are denoted by plus (+) signs and bond contractions and angle closings are denoted by minus (−) signs. [g] Overtone corresponding to 2 × 1357 cm^{-1}. [h] Combination bands corresponding to 1370 + 926 and 1357 + 924 cm^{-1}.

calculated frequencies and Raman intensities (Tables 3−5 and S4−S11) of the energy-minimized geometries (Figure 5) and, in the case of CH_3CN modes, by comparison with those of the free ligand and other CH_3CN adducts. The spectra of CH_3CN and $CH_3CN{\cdot}m$HF, prepared from a 2:1 molar ratio of HF and CH_3CN (no free CH_3CN was observed; also see NMR Spectroscopy), were also recorded at −150 °C and assigned (Tables S2 and S3) for comparison with those of $F_2{}^{16/18}OXeN{\equiv}CCH_3$.

Table 5. Experimental Vibrational Frequencies[a] for $F_2Xe^{16/18}O\cdot nHF$ and $F_2Xe^{16/18}O\cdot nDF$

exptl[b]				assgnts (C_1)	
$Xe^{16}OF_2\cdot nHF$	$Xe^{18}OF_2\cdot nHF$	$Xe^{16}OF_2\cdot nDF$	$Xe^{18}OF_2\cdot nDF$		
2854(<1), br	2854(<1), br	2164(1), br	2165(1), br	ν_1	ν(H[D]F) + minor ν(O···H[D]−F)
n.o.	n.o.	n.o.	n.o.	ν_2	δ(O···H[D]−F)
733.5(34)	696.4(25)	734.0(46)	697.3(27)	ν_3	ν(XeO)
n.o.	n.o.	n.o.	n.o.	ν_4	HF oop wag
n.o.	n.o.	n.o.	n.o.	ν_5	$\nu_{as}(XeF_2)$ + minor H[D]F oop wag
498.2(100)	497.7(100)	497.7(100)	497.7(100)	ν_6	$\nu_s(XeF_2)$
299.1(2)	294.8(1)	293.8(2)	289.8(2)	ν_7	$\delta(F_{H[D]}XeO)$
286.6(8)	276.4(8)	285.1(10)	275.9(8)	ν_8	$\rho_{rock}(XeOF_2)$ ip + minor H[D]F oop wag
200.2(2)	199.8(2)	201.2(2)	199.8(2)	ν_9	$\delta(XeF_2)$ oop
187.2(6)	186.3(6)	187.2(7)	186.3(7)		
166.0(5)	164.6(5)	165.5(6)	164.1(6)	ν_{10}	$\delta(XeF_2)$ ip
129.4(4)	127.0(11)	127.5(5) 119.3, sh	125.6(6)	ν_{11}	$\rho_{rock}(XeOF_2)$ oop + ν(H[D]F···Xe)
89.9(2)	89.8(2)				
65.3(1)	64.3(1)				
n.o.	n.o.	n.o.	n.o.	ν_{12}	XeF_2 torsion about Xe−O bond

[a] Frequencies are given in cm^{-1}. Abbreviations are given in footnotes f and a of Tables 3 and 4, respectively. [b] Raman spectra of $Xe^{16/18}OF_2\cdot nHF$ and $Xe^{16/18}OF_2\cdot nDF$ were recorded in an FEP sample tube at −150 °C using 1064-nm excitation. Values in parentheses denote relative Raman intensities. [c] Lattice modes and/or instrumental artifacts.

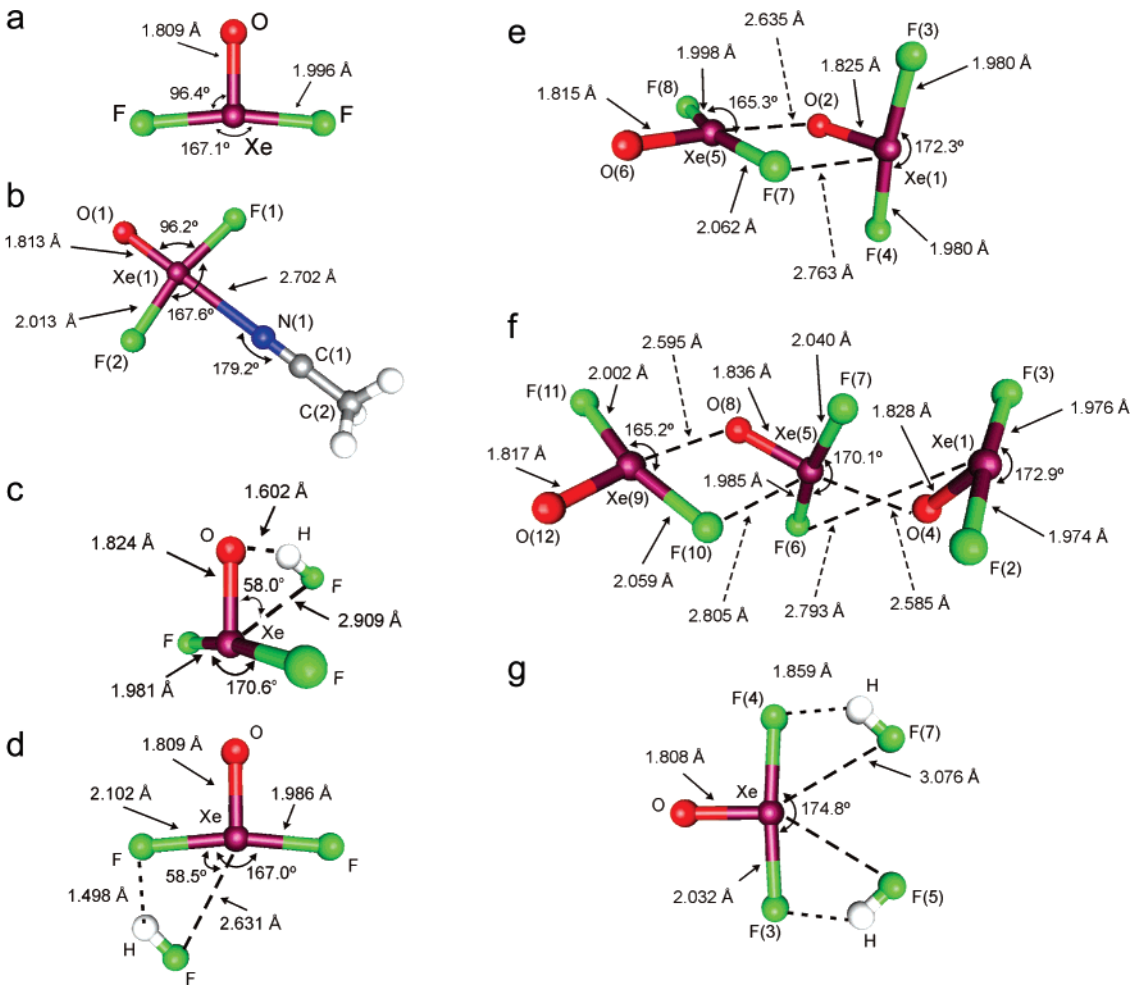

Figure 5. Calculated geometries (SVWN/(SDB-)cc-pVTZ) of (a) $XeOF_2$, (b) $F_2OXeN{\equiv}CCH_3$, (c) $XeOF_2\cdot HF$, O···H coordinated, (d) $XeOF_2\cdot HF$, F···H coordinated, (e) $(XeOF_2)_2$, (f) $(XeOF_2)_3$, and (g) $XeOF_2\cdot 2HF$.

Assignments of modes involving the oxygen and hydrogen atoms were also supported by experimental and calculated $^{16/18}O$ and $^{1/2}H$ isotopic shifts. Vibrational frequencies calculated at both the MP2 (values in parentheses in the present discussion and throughout) and SVWN levels of theory reproduced the observed frequency trends across the series of compounds.

(a) $XeOF_2$. The $XeOF_2$ molecule (C_{2v}) possesses six fundamental vibrational modes belonging to the irreducible representations $3A_1 + 2B_1 + B_2$ (the *xy*-plane is the molecular plane) that are Raman and infrared active. Although there is overall good agreement between the observed and calculated frequency trends for $XeOF_2$, the stretching frequencies are overestimated

whereas those of the deformation modes are slightly underestimated. Discrepancies are expected to arise, in part, because the low coordination number and large valence shell of xenon in $XeOF_2$ are conducive to association in the solid state.

The highest frequency mode at 749.9 cm^{-1} is assigned to the ν(XeO) stretch and displays a substantial low-frequency shift (37.1 cm^{-1} or 4.95%) upon substitution of ^{18}O and is in good agreement with the calculated percentage $^{16/18}O$ isotope shift [39.2 (46.6) cm^{-1} or 4.93 (4.96)%]. The mode at 298.1 cm^{-1} displays a smaller $^{16/18}O$ isotope shift of 9.1 cm^{-1} (3.05%) [calculated 9.3 (10.9) cm^{-1} or 3.81 (3.85)%] and is assigned to the in-plane $\rho_{rock}(XeOF_2)$ mode. Similar isotope shifts were observed and calculated for the $Xe^{16/18}OF_2 \cdot n^{1/2}HF$ and $F_2{}^{16/18}OXeN{\equiv}CCH_3$ adducts (vide infra). It is clear from the high frequency of ν(XeO) that the formal Xe−O bond order is close to two, ruling out the polymeric infinite chain structure, $[\text{-O}-Xe(F_2)\text{-}]_n$, predicted by Gillespie.[34] However, the calculated ν(XeO) and $\nu_s(XeF_2)$ frequencies of $XeOF_2$ are significantly higher than the experimental values, and the experimental frequencies are 9 and 20 cm^{-1}, respectively, lower than those of $F_2OXeN{\equiv}CCH_3$ (vide infra), suggesting that weak oxygen and/or fluorine coordination to adjacent xenon atoms occurs in the solid (cf. gas-phase dimer and trimer in the Computational Results).

As predicted from the calculated Raman intensities, the $\nu_s(XeF_2)$ stretch at 467.8 cm^{-1} is the most intense mode in the Raman spectrum. Because the XeF_2 moiety is near linear and near centro-symmetric, mutual exclusion applies. Thus, $\nu_{as}(XeF_2)$ is expected to be very weak and was not observed, but is predicted to occur at 572.3 (582.5) cm^{-1} compared to $\nu_{as}(XeF_4)$ of XeF_4 (586 cm^{-1}, infrared spectrum).[2] The weak modes at 251.4 and 256.2 cm^{-1} are assigned to the out-of-plane XeF_2 bending mode, and the bands at 154.0 and 175.7 cm^{-1} are assigned to the in-plane XeF_2 bending mode.

(b) $F_2OXeN{\equiv}CCH_3$. A solution sample of $F_2OXeN{\equiv}CCH_3$, generated in CH_3CN according to eq 1, was pumped under dynamic vacuum at −45 to −42 °C until a slurry of $F_2OXeN{\equiv}CCH_3$ wetted with CH_3CN had formed. Removal of the remaining CH_3CN and HF was then monitored by low-temperature Raman spectroscopy after every 5−10 min pumping interval. This permitted distinction and unambiguous assignment of the CH_3CN modes associated with the solvent, $F_2OXeN{\equiv}CCH_3$, and $CH_3CN \cdot m$HF [$\nu_{as}(CH_3)$, 3018.1; $\nu_s(CH_3)$, 2949.0; ν(CN), 2282.1, 2309.6; $\delta_{as}(CH_3)$, 1451.9; $\delta_s(CH_3)$, 1361.7; ν(CC), 932.5 cm^{-1}; also see Tables S1−S3].

All vibrational modes (24 A) of $F_2OXeN{\equiv}CCH_3$ (C_1) are predicted to be Raman and infrared active. The $\nu_s(CH_3)$, $\nu_{as}(CH_3)$, ν(CN), $\delta_{as}(CH_3)$, $\delta_s(CH_3)$, ν(XeO), $\nu_s(XeF_2)$, δ(CCN), and $\delta_{rock}(XeOF_2)$ ip bands are split into two to four components (Table 4). To account for these splittings, a factor-group analysis was performed based on the single-crystal X-ray structure. The analysis reveals that each Raman and infrared band is split, as a result of coupling within the unit cell, into a maximum of four components, $2A_g + 2B_g$ in the Raman spectrum and $2A_u + 2B_u$ in the infrared spectrum (Table S12).

The frequencies associated with the $XeOF_2$ moiety have been assigned by analogy with those of $XeOF_2$ as discussed above, and require no further commentary except to note that the $\nu_s(XeF_2)$ stretching frequency is shifted to higher frequency when compared with that of $XeOF_2$, which is also observed for the HF adduct (vide infra).

Table 4 shows that the $XeOF_2$ group modes are affected by adduct formation, with both the ν(XeO) and $\nu_s(XeF_2)$ modes being shifted to higher frequencies by 9 and 20 cm^{-1}, respectively. In contrast, the calculated frequencies indicate that $\nu_s(XeF_2)$ should decrease [19 (16) cm^{-1}] and that ν(XeO) should remain unchanged when adduct formation takes place in the gas phase. The discrepancy may result from $XeOF_2$ association in the solid state which likely occurs by means of asymmetric oxygen bridges (vide supra). Formation of the CH_3CN adduct presumably disrupts solid state association, forming discrete monomers, as shown in its crystal structure, resulting in increases in Xe−O bond order and ν(XeO).

In contrast with $XeOF_2$ and $XeOF_2 \cdot n$HF, the low symmetries of the two conformations observed for $F_2OXeN{\equiv}CCH_3$ in its crystal structure allow the $\nu_{as}(XeF_2)$ mode to be observed as a weak line at 525.2 cm^{-1}. The in-plane $\delta(XeF_2)$ deformation mode is symmetrically and antisymmetrically coupled to the ν(XeN) stretch, occurring at 147.9, 164.1 cm^{-1} [ν(XeN) + $\delta(XeF_2)$ ip] and 116.4, 133.7 cm^{-1} [ν(XeN) − $\delta(XeF_2)$ ip].

All frequencies associated with coordinated CH_3CN were readily assigned by comparison with those of the free base. The bands at 2253.7 and at 390.2, 392.6, and 397.4 cm^{-1} are assigned to the ν(CN) stretch and the δ(NCC) bend, respectively, and are shifted to higher frequencies when compared with those of the free ligand. The experimental ν(CN) (5.3 cm^{-1}) and δ(NCC) (2.1 cm^{-1}, average) complexation shifts are much smaller than those associated with other Lewis acid adducts of CH_3CN (CH_3CNSbF_5, 80 and 36 cm^{-1};[35] CH_3CNBF_3, 114 and 58 cm^{-1};[36] and CH_3CNBCl_3, 118 and 80 cm^{-1},[37] respectively), and are indicative of a comparatively weak donor−acceptor bond in $F_2OXeN{\equiv}CCH_3$. Whereas the calculated ν(CN) [15.2 (16.7) cm^{-1}] and δ(NCC) [8.9 (9.8) cm^{-1}) complexation shifts are much less, the ratios of the stretching to bending complexation shifts are similar.

(c) $XeOF_2 \cdot n$HF. When HF was added to $XeOF_2$ at −78 °C, a Raman spectrum that was more complex than that of $XeOF_2$ resulted, which was identical to that previously reported for, and erroneously assigned to, $XeOF_2$.[15] In an attempt to more fully understand the nature of the interaction between HF and $XeOF_2$, the deuterium substituted $^{16/18}O$ isotopomers were also synthesized.

When the Raman spectra of all four isotopomers are considered (Table 5), only one of the eight $XeOF_2 \cdot n$HF vibrational modes that could be observed exhibited both $^{16/18}O$ and $^{1/2}H$ dependencies that were >2 cm^{-1}. In addition, three modes exhibited only $^{16/18}O$ dependence, one mode exhibited only $^{1/2}H$ dependence (this mode is very broad, ∼100 cm^{-1}, and is not expected to exhibit a discernible $^{16/18}O$ isotope shift), and three were unshifted. To account for the isotopic dependencies of the experimental vibrational frequencies and to determine the manner in which HF is coordinated in $XeOF_2 \cdot n$HF, several simplified models were calculated (see Computational Results).

(34) Gillespie, R. J. In *Noble Gas Compounds*; Hyman, H. H., Ed.; The University of Chicago Press: Chicago, 1963; pp 333−339.

(35) Von Ahsen, B.; Bley, B.; Proemmel, S.; Wartchow, R.; Willner, H.; Aubke, F. *Z. Anorg. Allg. Chem.* **1998**, *624*, 1225−1234.
(36) Swanson, B.; Shriver, D. F. *Inorg. Chem.* **1970**, *9*, 1406−1416.
(37) Swanson, B.; Shriver, D. F. *Inorg. Chem.* **1971**, *10*, 1354−1365.

The vibrational assignments for $Xe^{16/18}OF_2 \cdot n^{1/2}HF$ were based upon a comparison of two energy-minimized structures in which a single HF molecule coordinates to $XeOF_2$. In one case, the HF molecule occupies a plane perpendicular to the $XeOF_2$ plane and is coordinated to xenon through fluorine and is cis to the oxygen atom so that HF is hydrogen-bonded to oxygen (Figure 5c). The second energy-minimized model (Figure 5d) in which HF is also fluorine-coordinated to xenon differs in that HF is hydrogen-bonded to the fluorine on xenon and lays in the $XeOF_2$ plane. The latter structure is favored by 7.8 (1.6) kJ mol^{-1} over the O···H-bonded structure in Figure 5c.

The O···H-bonded model, in which bicoordinate HF increases the xenon coordination number by bonding through fluorine, gives twelve modes: five $^{16/18}$O- and $^{1/2}$H-dependent modes (ν_1, ν_2, ν_4, ν_7, ν_8), one $^{16/18}$O-dependent mode (ν_3), one $^{1/2}$H-dependent mode (ν_5), and five unshifted modes (ν_6, ν_9-ν_{12}). In contrast, the F···H-bonded structure gives one $^{16/18}$O- and $^{1/2}$H-dependent mode (ν_1), two $^{16/18}$O-dependent modes (ν_3, ν_8), three $^{1/2}$H-dependent mode (ν_2, ν_4, ν_7), and six (ν_5, ν_6, ν_9-ν_{12}) unshifted modes. Overall, the calculated vibrational frequencies derived from the slightly less stable O···H-bonded structure, when compared with the calculated $XeOF_2$ and $F_2OXeN{\equiv}CCH_3$ frequencies, best reproduces the experimental frequency trends and isotopic shift patterns. Consequently, the ensuing vibrational assignments and descriptions (Table 5) are based on this structure.

The modes at 2854 and 2164 cm^{-1} are readily assigned to ν(HF) and ν(DF), where their lower frequencies relative to those in a neon matrix (HF 3992; DF 2924 cm^{-1})[38] and in the solid phase (HF 3056, 3408; DF 2284, 2524 cm^{-1})[39,40] are consistent with coordinated HF and DF. The ν(XeO) stretching frequency of $XeOF_2 \cdot n$HF (733.5 cm^{-1}) shows the expected $^{16/18}$O isotopic dependence and is shifted to lower frequency relative to that of $XeOF_2$ (749.9 cm^{-1}). The most intense mode at 498.2 cm^{-1} corresponds to $\nu_s(XeF_2)$, which is comparable to that in $F_2OXeN{\equiv}CCH_3$ (481.8, 488.1, 494.4, 499.1 cm^{-1}) but higher than in $XeOF_2$ (467.8 cm^{-1}). The asymmetric mode $\nu_{as}(XeF_2)$ is again expected to be very weak and was not observed. Upon ^{18}O enrichment, the modes at 286.6 and 299.1 cm^{-1} shift to 276.4 and 294.8 cm^{-1}, respectively. Upon ^{2}H enrichment, these modes shift to even lower frequencies by 1.5 and 5.1 cm^{-1}, respectively, and are assigned to $\rho_{rock}(XeOF_2)$ ip + minor HF oop wag and $\delta(F_HXeO)$, respectively. The in-plane XeF_2 (166.0 cm^{-1}) and the out-of-plane XeF_2 (187.2, 200.2 cm^{-1}) bends are shifted to higher and lower frequency, respectively, when compared with those of $XeOF_2$ and show only small (<2 cm^{-1}) $^{16/18}$O isotopic dependencies. The band at 129.4 cm^{-1} shifts to lower frequency upon ^{2}H (≥2 cm^{-1}) and ^{18}O (<2 cm^{-1}) enrichment and is assigned to a coupled mode involving the coordinated HF molecule, $\rho_{rock}(XeOF_2)$ oop + ν(HF···Xe).

An energy-minimized structure for $XeOF_2 \cdot 2HF$ was also obtained, but provided vibrational frequencies that were in poor agreement with the experimental values (see Computational Results).

Computational Results. The electronic structures of $(Xe^{16/18}OF_2)_n$ (n = 1−3), $F_2{}^{16/18}OXeN{\equiv}CCH_3$, and $Xe^{16/18}OF_2 \cdot n^{1/2}HF$ (n = 1, 2) were optimized starting from C_1 symmetries and resulted in stationary points with all frequencies being real. Only the SVWN/(SDB-)cc-pVTZ and MP2/(SDB-)cc-pVTZ (MP2 values in the present discussion are given in parentheses) results are reported in this paper (Tables 2−4, Figure 5 and Tables S4−S11; S13; also see Experimental Section). Xenon tetrafluoride was used to benchmark the calculations (Table S14).

(a) Geometries. (i) $(XeOF_2)_n$ (n = 1−3). The geometry of $XeOF_2$ optimized to C_{2v} symmetry with an Xe−O bond length of 1.809 (1.770) Å and Xe−F bond length of 1.996 (1.980) Å, compared to 1.971 (1.960) Å in XeF_4 and its experimental bond length, 1.953(2) Å.[4] The fluorine atoms are bent away from the oxygen atom, with an O−Xe−F angle of 96.4 (96.0)° and an F−Xe−F angle of 167.1 (168.2)°. The calculated structure is in accord with that predicted by the VSEPR model of molecular geometry (see Raman Spectroscopy).

The geometries of $(XeOF_2)_2$ and $(XeOF_2)_3$ were also calculated (Tables S10 and S11) to study the effects of oligomerization on the vibrational frequencies and to assess the relative merits of $XeOF_2$ association in the solid state. In both cases, two starting models were used with all Xe−O bonds collinear: one with all $XeOF_2$ groups coplanar, as originally proposed by Gillespie,[34] and one with the $XeOF_2$ planes alternating so that they subtend dihedral angles of 90°. All systems converged to a single twisted dimer (Figure 5e) and open-chain, twisted trimer (Figure 5f). Both the dimer and trimer possess Xe···O and Xe···F contacts that are significantly less than the sums of the van der Waals radii (3.68 and 3.63 Å, respectively).[28] The formal Xe−O double bond involved in the contact elongates, allowing the F−Xe−F angle to open up. As well, the Xe−F bonds elongate and both ν(XeO) and $\nu_s(XeF_2)$ decrease significantly relative to those of the calculated monomer.

(ii) $F_2OXeN{\equiv}CCH_3$. The geometry of $F_2OXeN{\equiv}CCH_3$ optimized to C_1 symmetry in which the NCC moiety lay in the $XeOF_2$ plane and the Xe−N−C angle is nearly linear. Overall there is a good agreement between the observed and the calculated Xe−O and Xe−F bond lengths as well as the F−Xe−F and O−Xe−F bond angles (Table 2). The most notable differences occur between the observed and calculated Xe−N−C bond angle and Xe−N bond length. The Xe−N bond length, which is slightly underestimated by the SVWN calculation, has a calculated value of 2.702 (2.884) Å when compared with 2.752(5) (out-of-plane conformer) and 2.808(5) (in-plane conformer) Å in the crystal structure. Unlike the experimental Xe−N−C bond angles (164.9(4)°, in-plane conformer; and 134.6(4)°, out-of-plane conformer), the calculated Xe−N−C angle is essentially linear [179.2 (179.4)]. The energies of the two experimental adduct conformations were calculated at the MP2 level and are 78.2 (out-of-plane) and 86.9 (in-plane) kJ mol^{-1} higher in energy than the energy-minimized geometry. The conformational differences in the solid state are likely a consequence of crystal packing.

Upon adduct formation, the calculated Xe−O bond length (1.809−1.813 Å) and ν(XeO) remain essentially unchanged. The XeF bond lengths are elongated (1.996−2.013 Å) and the ν(XeF) decreases accordingly. In contrast, the experimental ν(XeO) and ν(XeF) frequencies increase (Tables 3 and 4).

(iii) $XeOF_2 \cdot n$HF (n = 1, 2). Because an experimental structure for $XeOF_2 \cdot n$HF is unavailable, it was not possible to directly establish the number of HF molecules coordinated to

(38) Mason, M. G.; Von Holle, W. G.; Robinson, D. W. *J. Chem. Phys.* **1971**, *54*, 3491−3499.
(39) Kittelberger, J. S.; Hornig, D. F. *J. Chem. Phys.* **1967**, *46*, 3099−3108.
(40) Tubino, R.; Zerbi, G. *J. Chem. Phys.* **1969**, *51*, 4509−4514.

Table 6. Natural Bond Orbital (NBO) Charges, Valencies, and Bond Orders for $XeOF_2$, $F_2OXeN{\equiv}CCH_3$, and CH_3CN

	$XeOF_2$				$F_2OXeN{\equiv}CCH_3$				CH_3CN			
	SVWN		MP2		SVWN		MP2		SVWN		MP2	
					Charges [Valencies]							
Xe(1)	1.971	[1.478]	2.112	[1.473]	2.011	[1.437]	2.065	[1.450]				
O(1)	−0.807	[0.777]	−0.897	[0.782]	−0.853	[0.722]	−0.887	[0.754]				
F(1)	−0.582	[0.317]	−0.608	[0.304]	−0.598	[0.277]	−0.599	[0.286]				
F(2)	−0.582	[0.317]	−0.608	[0.304]	−0.598	[0.277]	−0.599	[0.286]				
N(1)					−0.410	[2.035]	−0.405	[1.988]	−0.310	[1.958]	−0.313	[1.892]
C(1)					0.374	[3.014]	0.359	[2.979]	0.271	[3.014]	0.283	[2.879]
C(2)					−0.791	[3.295]	−0.781	[3.288]	−0.786	[3.299]	−0.678	[3.290]
H					0.288	[0.786]	0.283	[0.791]	0.275	[0.788]	0.236	[0.805]
					Bond Orders							
Xe(1)−O(1)	0.812		0.825		0.752		0.789					
Xe(1)−F(1)	0.333		0.324		0.290		0.301					
Xe(1)−F(2)	0.333		0.324		0.290		0.301					
O(1)···F(1)	−0.017		−0.021		−0.015		−0.017					
Xe(1)···N(1)					0.099		0.059					
N(1)−C(1)					1.926		1.924		1.951		1.882	
C(1)−C(2)					1.024		1.000		1.012		0.951	
C(2)-H					0.753		0.760		0.758		0.775	

$XeOF_2$. Energy-minimized structures and their vibrational frequencies were calculated to better comprehend how HF interacts with $XeOF_2$. It was decided to limit the models to a $XeOF_2$ monomer interacting with only one or two HF molecules. These results are given in Tables S4−S9.

Four starting geometries were used in which a single HF molecule, H-bonded to either oxygen or fluorine, lay either in the $XeOF_2$ plane and collinear with the Xe−O bond, or perpendicular to the $XeOF_2$ plane. A single energy-minimized structure was found for each pair of O···H−F and F···H−F bonded starting geometries. In both minimized geometries, the fluorine of HF is coordinated to xenon. In the F···H−F···Xe structure, the HF molecule lies in the $XeOF_2$ plane (Figure 5d), and in the O···H−F···Xe structure, it occupies the plane perpendicular to the $XeOF_2$ plane (Figure 5c). Although the F···H−F···Xe structure is 7.8 (1.6) kJ mol^{-1} more stable than the O···H−F···Xe structure, the calculated frequencies of the latter are in better agreement with the experimental frequencies (see Raman Spectroscopy). In the O···H structure, both the Xe−O bond length and F−Xe−F axial bond angle increase when compared with those of $XeOF_2$, whereas the Xe−F bond lengths decrease. In the F···H structure, both the Xe−O bond length and the F−Xe−F bond angle remain unchanged, whereas the Xe−F bond involved in the F···H contact increases and the other Xe−F bond decreases. In both cases, the O···H and F···H distances are significantly shorter than the sum of their respective van der Waals radii.

Initial geometries in which two HF molecules were orientated in or out of the $XeOF_2$ plane and were H···O or H···F coordinated or had mixed H···O/H···F coordination for both orientations were used. Of these ten initial geometries, only one energy-minimized geometry having non-imaginary frequencies was obtained. This geometry has two F···H−F and two Xe···F−H interactions that lie in the $XeOF_2$ plane (Figure 5g). Both the Xe−F distance and F−Xe−F angle have increased relative to that of $XeOF_2$ whereas Xe−O has decreased. The Xe···F and F···H contact distances are significantly longer than those in the calculated structure containing one coordinated HF molecule (Figure 5d). The geometry calculated for $XeOF_2{\cdot}2HF$, however, provided vibrational frequencies that were in poor agreement with the experimental values (Tables S8 and S9).

(b) Natural Bond Orbital (NBO) Analyses. The NBO[41−44] analyses were carried out for the MP2- and SVWN-optimized gas-phase geometries of $XeOF_2$, $F_2OXeN{\equiv}CCH_3$, and CH_3CN. The NBO results are given in Table 6. The MP2 and SVWN results are similar; only the MP2 results are referred to in the ensuing discussion. Single point calculations were carried out for geometries that were constrained to those of the experimental conformers and reveal that the NBO analyses (Table S15) are very similar to that of the fully optimized C_1 structure and insensitive to the Xe−N−C bond angle.

The NBO analyses give natural charges of 2.11 and 2.06 for Xe in $XeOF_2$ and $F_2OXeN{\equiv}CCH_3$, respectively. These charges, which are approximately the average of the formal charge 0 (covalent model) and formal oxidation number 4 (ionic model) for Xe in both molecules, are in accord with the natural charges for O (−0.90, −0.89) and F (−0.61, −0.60) in $XeOF_2$ and $F_2OXeN{\equiv}CCH_3$, respectively. In both cases, the charges are also about half of their respective oxidation numbers, and indicate that the bonds in free and adducted $XeOF_2$ are polar covalent. Among the plausible valence structures I−IV for $XeOF_2$, the calculated charges are best represented by structure IV, where the near linear XeF_2 moiety can be described as a 3 center-4 electron bond.[45] The Xe−O/Xe−F bond order ratio (2.55) and Xe/O/F valencies (1.47/0.78/0.30) are in overall agreement with this localized description of polar covalent bonding in $XeOF_2$.

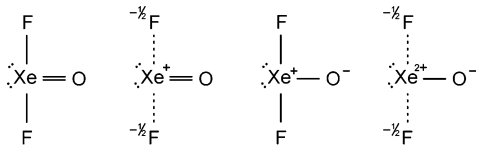

I **II** **III** **IV**

Upon adduct formation with CH_3CN, the nitrogen electron pair density donated into the xenon valence shell results in essentially no change in the O and F ligand charges but small

(41) Reed, A. E.; Weinstock, R. B.; Weinhold, F. *J. Chem. Phys.* **1985**, *83*, 735−746.
(42) Reed, A. E.; Curtiss, L. A.; Weinhold, F. *Chem. Rev.* **1998**, *88*, 899−926.
(43) Glendening, E. D.; Reed, A. E.; Carpenter, J. E.; Weinhold, F. *NBO Version 3.1*; Gaussian Inc.: Pittsburgh, PA, 1990.

decreases in their bond orders and valencies, whereas Xe maintains its positive charge very close to 2. Thus, the Xe−O and Xe−F bonds are only slightly more ionic in $F_2OXeN{\equiv}CCH_3$. The charge distribution of the CN group is polarized toward the positive xenon center, with 0.10 e charge shifting from carbon to nitrogen upon coordination with a corresponding polarization of charge on the CH_3 group toward the positively charged carbon atom of the CN group.

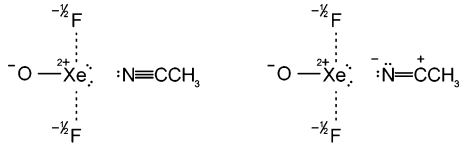

V

VI

The most plausible valence bond contributions that contribute to a description of $F_2OXeN{\equiv}CCH_3$ are those that retain the charge distribution and Xe−O and Xe−F bond orders of structure IV and also account for the very low Xe−N bond order (0.05) and polarization of the CH_3CN ligand to give an enhanced negative charge on nitrogen. These criteria are met by valence structures V and VI, where structure V is dominant and yields a picture of adduct formation between $XeOF_2$ and CH_3CN that is similar to that of XeF^+ and HCN.[46] In this depiction, mutual penetration of outer diffuse nonbonded densities of the Xe and N atoms occurs which, unlike a covalent interaction, produces no substantial shared density as reflected in the very low Xe−N bond order and small changes in Xe and N valencies.

The calculated gas-phase xenon-ligand dissociation energy for $F_2OXeN{\equiv}CCH_3$ at the MP2 level of theory is 41.8 kJ mol^{-1}, which is significantly less than the donor−acceptor adduct dissociation energies of $F_3S{\equiv}NXeF^+$ (157.2 kJ mol^{-1}) and $HC{\equiv}NXeF^+$ (157.1 kJ mol^{-1}).[32] The $F_2OXeN{\equiv}CCH_3$ donor−acceptor interaction is in better agreement with those calculated for $HC{\equiv}NAsF_5$ (38.6 kJ mol^{-1}) and $F_3S{\equiv}NAsF_5$ (27.8 kJ mol^{-1}).[32] These findings also support a valence bond description of $F_2OXeN{\equiv}CCH_3$ that is dominated by the nonbonded structures V and VI and a bonding description in which $CH_3C{\equiv}N$ is weakly coordinated to $XeOF_2$.

Conclusion

Long-standing discrepancies among the published vibrational assignments ascribed to $XeOF_2$ are now accounted for and the synthesis of pure $XeOF_2$ in synthetically useful quantities has been achieved. Comparisons of the present experimental frequencies for $XeOF_2$ and $XeOF_2{\cdot}n$HF with those assigned to $XeOF_2$ in the previous three early communications[13−15] show that the spectra obtained from H_2O/XeF_4 co-condensation experiments[13,14] arose from mixtures of $XeOF_2{\cdot}n$HF and $XeOF_2$ while the product described in the latter report[15] consisted of only $XeOF_2{\cdot}n$HF. In these accounts, HF produced in the co-condensation reactions either coordinated to $XeOF_2$ or was pumped off, yielding mixtures of $XeOF_2{\cdot}n$HF and $XeOF_2$ that were erroneously ascribed to a single component, $XeOF_2$.

The solid-state vibrational spectrum of $XeOF_2$ and the calculated energy-minimized dimer and trimer geometries, and their vibrational frequencies, point to an extended structure in which neighboring $XeOF_2$ molecules weakly interact by means of asymmetric oxygen-xenon-oxygen bridges and Xe···F contacts.

The Lewis acid properties of $XeOF_2$ are demonstrated by the syntheses of $F_2OXeN{\equiv}CCH_3$ and $XeOF_2{\cdot}n$HF. The crystal structure of $F_2OXeN{\equiv}CCH_3$ provides a rare example of a Xe(IV)−N bond which is among the weakest Xe−N bonds known. It has been shown by calculation of energy-minimized structures of $XeOF_2{\cdot}$HF and $XeOF_2{\cdot}$2HF, in combination with calculated and experimental vibrational frequencies resulting from $^{16/18}O$ and $^{1/2}H$ isotopic substitution, that most likely $n = 1$, and that HF, in this instance, is coordinated to $XeOF_2$ by means of weak O···H and Xe···F bonds.

The present syntheses of $XeOF_2$ and its HF and CH_3CN adducts, along with their detailed structural characterizations, represent a significant extension of Xe(IV) chemistry and account for most of what is presently known about the oxide fluoride chemistry of Xe(IV). The present findings may be expected to facilitate the extension of Xe(IV) oxide fluoride chemistry into areas such as the fluoride ion donor−acceptor properties of $XeOF_2$ and derivatives with other highly electronegative ligands, as well as offer the possibility to synthesize presently unknown XeO_2.

Experimental Section

Caution: *Anhydrous HF must be handled using appropriate protective gear with immediate access to proper treatment procedures[47−49] in the event of contact with liquid HF, HF vapor, or HF-containing solutions. All Xe(IV) oxide fluoride species dealt with in the present study, namely, $XeOF_2$, $F_2OXeN{\equiv}CCH_3$, and $XeOF_2{\cdot}n$HF are highly energetic materials and are only stable at the low temperatures employed in the experimental procedures outlined below. All detonate upon warming. Thus, adequate protective apparel and working behind adequate shielding are crucial for the safe manipulation of these materials. In the case of $XeOF_2$, detonations may also occur upon freezing or further cooling of its CH_3CN solutions/suspensions to −196 °C. It is therefore strongly recommended that syntheses of the aforementioned compounds be carried out on a small scale (<100 mg).*

Apparatus and Materials. (a) General. All manipulations involving air-sensitive materials were carried out under strictly anhydrous conditions as previously described.[50] Reaction vessels/Raman sample tubes and NMR sample tubes were fabricated from $^1/_4$-in. o.d and 4-mm o.d. FEP tubing, respectively, and outfitted with Kel-F valves. All reaction vessels and sample tubes were rigorously dried under dynamic vacuum prior to passivation with 1 atm of F_2 gas.

Acetonitrile (Caledon, HPLC grade) was purified by the literature method[51] and transferred under static vacuum on a glass vacuum line. Xenon tetrafluoride, was prepared and purified according to the literature method.[52] Anhydrous HF

(44) Glendening, E. D.; Badenhoop, J. K.; Reed, A. E.; Carpenter, J. E.; Bohmann, C. M.; Morales, C. M.; Weinhold, F. *NBO Version 5.0*; Theoretical Chemistry Institute, University of Wisconsin: Madison, WI, 2001.
(45) Christe, K. O. In *XXIVth International Congress of Pure and Applied Chemistry*; Butterworth: London, 1974; Vol. 4, p 115.
(46) MacDougall, P. J.; Schrobilgen, G. J.; Bader, R. F. W. *Inorg. Chem.* **1989**, *28*, 763−769.
(47) Bertolini, J. C. *J. Emerg. Med.* **1992**, *10*, 163−168.
(48) Peters, D.; Mietchen, R. *J. Fluorine Chem.* **1996**, *79*, 161−165.
(49) Segal, E. B. *Chem. Health Saf.* **2000**, 18−23.
(50) Casteel, W. J., Jr.; Dixon, D. A.; Mercier, H. P. A.; Schrobilgen, G. J. *Inorg. Chem.* **1996**, *35*, 4310−4322.
(51) Winfield, J. M. *J. Fluorine Chem.* **1984**, *25*, 91−98.
(52) Chernick, C. L.; Malm, J. G. *Inorg. Synth.* **1966**, *8*, 254−258.

(Harshaw Chemicals Co.) was purified by the standard literature method.[53] Both H_2O (Caledon, HPLC grade) and $H_2{}^{18}O$ (Isotec, 98.6 atom % ^{18}O) were used without further purification to prepare 2.00 M $H_2{}^{16/18}O$ solutions in CH_3CN. An ^{17}O-enriched sample of H_2O (Office de Rayonnements Ionisants, Saclay, France; 35.4% ^{16}O, 21.9% ^{17}O, 42.7% ^{18}O) was used to prepare a CH_3CN solution of $XeOF_2$ for ^{17}O NMR studies. High-purity Ar or N_2 gases were used for backfilling vessels.

(b) DF. Deuterium fluoride was prepared by the reaction of D_2SO_4 with CaF_2. The detailed synthesis is provided in the Supporting Information.

(c) $F_2{}^{16/18}OXeN{\equiv}CCH_3$. In a typical synthesis, 60.6 mg of XeF_4 was added, inside a drybox, to a $^1/_4$-o.d. FEP reaction tube attached to a $^1/_4$-in stainless steel Swagelok Ultra-Torr union fitted with Viton O-rings which was, in turn, attached to a Kel-F valve through a short length of thick-wall $^1/_4$-in o.d. FEP tubing that was compression fitted to the valve. The reactor was disassembled outside the drybox at the union and quickly replaced with a Kel-F plug having two $^1/_{16}$-in holes drilled through its top which opened into the reaction vessel. A $^1/_{16}$-in Teflon tube, with a slow stream of dry argon passing through it, was threaded through one hole and positioned well above the XeF_4. This permitted the nitrogen in the tube to be displaced with argon through the second hole in the Kel-F plug. The tube was cooled to −78 °C while maintaining the argon flow. The argon flow was halted and 150 μL of 2.00 M solution of $H_2{}^{16/18}O$ in CH_3CN was syringed into the reactor through the argon outlet hole and frozen on the walls of the reaction vessel to give a 3−5% stoichiometric excess of $H_2{}^{16/18}O$. The solution was melted onto the XeF_4 at −42 °C and thoroughly mixed, resulting in the immediate formation of a yellow solution and precipitate. The solution was cooled to −45 °C whereupon more yellow solid precipitated. The union and valve assembly was reconnected and the solvent was immediately removed at temperatures between −45 to −42 °C under dynamic vacuum, leaving a pale yellow microcrystalline powder. Completeness of solvent removal was monitored by Raman spectroscopy (Table S1).

(d) $Xe^{16/18}OF_2$. A 66.1 mg sample of $F_2{}^{16/18}OXeN{\equiv}CCH_3$ was pumped under dynamic vacuum for 5 h with frequent agitation while maintaining the sample between −45 to −42 °C. This resulted in a bright yellow powder corresponding to $Xe^{16/18}OF_2$, which was shown to be free of coordinated CH_3CN by Raman spectroscopy (−150 °C). The compound is stable indefinitely when stored at −78 °C.

A solution of ^{17}O-enriched $XeOF_2$ in CH_3CN was prepared for ^{17}O NMR spectroscopy by in situ hydrolysis of XeF_4 (0.0219 g, 0.106 mmol) with ^{17}O-enriched H_2O (2.0 μL, 0.10 mmol) at −45 °C in a 4-mm o.d. FEP NMR tube.

(e) $Xe^{16/18}OF_2{\cdot}n^{1/2}HF$. Approximately 0.3 mL of anhydrous $^{1/2}HF$ was distilled into an evacuated reactor containing 54.1 mg of freshly prepared $Xe^{16/18}OF_2$ and frozen on the vessel walls at −196 °C.

Caution: *If condensation is too rapid and liquid HF condenses directly onto $XeOF_2$, rapid decomposition/detonation is likely to occur.* The $^{1/2}HF$ was melted onto the $Xe^{16/18}OF_2$ sample at −78 °C and was frequently mixed, over a 12−72 h period, by suspending the entire sample in $^{1/2}HF$ at this temperature and periodically monitored by recording the Raman spectrum of $Xe^{16/18}OF_2$/ $Xe^{16/18}OF_2{\cdot}n^{1/2}HF$ under a frozen layer of $^{1/2}HF$. Once solvation was complete, the resulting very pale yellow powder was isolated by removal of the $^{1/2}HF$ solvent under dynamic vacuum at −78 °C.

X-ray Crystallography. (a) Crystal Growth. Crystals of $F_2OXeN{\equiv}CCH_3$ were grown as previously described[54] by slow cooling of a CH_3CN solution of $XeOF_2$, previously saturated at ca. −35 °C, from −35 to −45 °C over the course of 5 h in a $^1/_4$-in o.d. FEP reactor as described in the synthesis of $F_2OXeN{\equiv}CCH_3$. When crystal growth was deemed complete, the reactor was maintained at −45 °C and was disassembled at the Swagelok Ultra-Torr union and quickly replaced with a Kel-F plug and $^1/_{16}$-in Teflon tube which had a slow steam of argon slowly passing through it (see the synthesis of $F_2OXeN{\equiv}CCH_3$). A second Teflon capillary tube was inserted through the outlet hole of the Kel-F cap while maintaining the argon flow. Lowering the outlet tube into the solution expelled the yellow supernatant through it into a second $^1/_4$-in o.d. FEP tube cooled to −78 °C. The union and valve assembly was replaced and the crystals were dried under dynamic vacuum at −45 to −42 °C and stored at −78 °C until a suitable crystal could be selected and mounted on the diffractometer. In addition to having a propensity to twin, the crystalline adduct proved difficult to handle because dry samples exploded at temperatures approaching 0 °C and had a tendency to slowly loose CH_3CN under dynamic vacuum at −45 °C (see Syntheses and Properties of $XeOF_2$, $F_2OXeN{\equiv}CCH_3$, and $XeOF_2{\cdot}n$HF). Crystalline $F_2OXeN{\equiv}CCH_3$ and its solutions were handled under low lighting conditions throughout crystal growth, crystal mounting, and data collection to minimize photodecomposition.

(b) Crystal Mounting. The sample tube was inserted into a hole drilled into a copper cylindrical block that had been previously cooled to −78 °C. The cold block covered the entire length of the sample tube to prevent warming and detonations of individual crystals as they were dumped into a crystal mounting trough cooled to −110 ± 5 °C by a cold stream of dry N_2 gas. This allowed selection of individual crystals from the bulk sample as previously described.[55] A single crystal of $F_2OXeN{\equiv}CCH_3$ was mounted on a glass fiber at −110 ± 5 °C using a Fomblin oil as the adhesive. The crystal used for data collection was a pale-yellow transparent plate measuring 0.20 × 0.20 × 0.12 mm.

(c) Collection and Reduction of X-ray Data. The single crystal was centered on a P4 Siemens diffractometer, equipped with a Siemens SMART[56] 1K charge-coupled devise (CCD) area detector (using the program SMART) and a rotating anode using graphite-monochromated Mo−K_α radiation (λ = 0.71073 Å). The diffraction data collection consisted of full ψ-rotation at χ = 0° (using 1040 + 80) 0.35° frames, followed by a series of short (80 frames) ω scans at various ψ and χ settings to fill the gaps. The crystal-to-detector distance was 4.994 cm, and the data collection was carried out in a 512 × 512 pixel mode using 2 × 2 pixel binning. Processing was carried out by using the program SAINT,[56] which applied Lorentz and polarization corrections to three-dimensionally

(53) Emara, A. A. A.; Schrobilgen, G. J. *Inorg. Chem.* **1992**, *31*, 1323−1332.
(54) Lehmann, J. F.; Dixon, D. A.; Schrobilgen, G. J. *Inorg. Chem.* **2001**, *40*, 3002−3017.
(55) Gerken, M.; Dixon, D. A.; Schrobilgen, G. J. *Inorg. Chem.* **2000**, *39*, 4244−4255.
(56) *SMART*, release 5.611, and *SAINT*, release 6.02; Siemens Energy and Automotive Analytical Instrumentation, Inc.: Madison, WI, 1999.

integrated diffraction spots. The program SADABS[57] was used for scaling the diffraction data, the application of a decay correction, and an empirical absorption correction based on redundant reflections.

(d) Solution and Refinement of the Structures. The XPREP[58] program was used to confirm the unit cell dimensions and the crystal lattice. The structure was solved in the space group $P2_1/c$ by use of direct methods and the solution yielded the positions of all the atoms, except for the hydrogen atoms, whose positions were calculated. Although a relatively satisfactory model could be obtained, the refinement as a single-crystal remained at an overall agreement factor of about 32%, with unsatisfactory behavior for some parameters. With the introduction of the twin matrix $(10\bar{1}0\bar{1}000\bar{1})$ characteristic of a pseudomerohedral twin, the refinement converged. The volume fractions of the twin individuals are $t_I = 0.87$ and $t_{II} = 0.13$. The final refinement was obtained by introducing anisotropic parameters for all the atoms, except the hydrogen atoms, an extinction parameter, and the recommended weight factor. The maximum electron densities in the final difference Fourier maps were located around the xenon atoms. The PLATON program[59] could not suggest additional or alternative symmetries.

NMR Spectroscopy. (a) Instrumentation. Nuclear magnetic resonance spectra of ^{19}F and ^{129}Xe were recorded unlocked (field drift <0.1 Hz h^{-1}) on a Bruker DRX-500 spectrometer equipped with an 11.744-T cryomagnet. For low-temperature work, the NMR probe was cooled using a nitrogen flow and variable-temperature controller (BV−T 3000). Fluorine-19 NMR spectra were acquired using a 5-mm combination $^1H/^{19}F$ probe operating at 470.593 MHz and ^{129}Xe NMR spectra were obtained using a 5-mm broad-band inverse probe operating at 139.051 MHz. Spectra were recorded in 32K (^{19}F) and 16K (^{129}Xe) memories, with spectral width settings of 25 (^{19}F) and 20 (^{129}Xe) kHz, yielding a data-point resolutions of 0.76 (^{19}F) and 2.44 (^{129}Xe) Hz/data point and acquisition times of 0.66 (^{19}F) and 0.41 (^{129}Xe) s. Pulse widths (μs), corresponding to bulk magnetization tip angles of approximately 90°, were 1.00 (^{19}F) and 18.0 (^{129}Xe). Relaxation delays of 0 (^{19}F) and 0.1 (^{129}Xe) s were used, and 200 (^{19}F) and 1000 (^{129}Xe) transients were accumulated. Line broadenings of 0 (^{19}F) and 2 (^{129}Xe) Hz were used in the exponential multiplication of the free induction decays prior to Fourier transformation. The ^{19}F and ^{129}Xe spectra were referenced externally at 30 °C to samples of neat $CFCl_3$ and $XeOF_4$, respectively. The chemical shift convention used is that a positive (negative) sign indicates a chemical shift to high (low) frequency of the reference compound.

(b) NMR Sample Preparation. Samples were prepared in $^1/_4$-in FEP tubes as described above for $F_2OXeN{\equiv}CCH_3$. The reactor was maintained at −42 to −45 °C and the solution was transferred into a 4-mm o.d. FEP tube fused to a $^1/_4$-in FEP tube that had been cooled to −78 °C and attached to a two-hole Kel-F plug. The transfer was carried out in a manner similar to that used for removal of the supernatant when isolating crystals of $F_2OXeN{\equiv}CCH_3$ for X-ray structure determination (see Crystal Growth). The union and valve assembly was replaced and the reactor was attached to a vacuum manifold where the NMR sample tube was cooled to −196 °C and heat-sealed under dynamic vacuum and stored at −78 °C until NMR spectra could be obtained. Samples were dissolved just prior to data acquisition at or below the temperature used to record their spectra. When obtaining low-temperature spectra, the 4-mm o.d. FEP tubes were inserted into 5-mm o.d. thin wall precision glass NMR tubes (Wilmad).

Raman Spectroscopy. Raman spectra were recorded on a Bruker RFS 100 FT-Raman spectrometer at −150 °C using 1064-nm excitation, 300 mW laser power and 1 cm^{-1} resolution as previously described.[55]

Computational Results. The optimized geometry and frequencies of $XeOF_2$ were initially calculated at the B3LYP, SVWN, and MP2 levels of theory using 321G, SDDAll (Stuttgart), DZVP and (SDB-)cc-pVTZ (i.e., cc-pVTZ for H, C, N, O, F, and SDB-cc-pVTZ for Xe) basis sets.[60] One calculation was also performed using CCSD(T)/(SDB-)cc-pVTZ, but it proved to be very time consuming and did not provide significantly better results. The results for (SDB-)cc-pVTZ and (SDB-)cc-pVQZ were very similar. The frequencies with the DZVP basis set were in good agreement with experiment, but the Xe−O and Xe−F bond lengths were overestimated. The optimized geometries and frequencies for $Xe^{16/18}OF_2$, $F_2{}^{16/18}OXeN{\equiv}CCH_3$, $Xe^{16/18}OF_2{\cdot}n^{1/2}HF$ and $Xe^{16/18}OF_2{\cdot}2^{1/2}HF$, $(Xe^{16/18}OF_2)_2$ dimer, and $(Xe^{16/18}OF_2)_3$ trimer were therefore calculated using SVWN/(SDB-)cc-pVTZ and MP2/(SDB-)cc-pVTZ. The NBO analyses[41−44] were performed for the SVWN and MP2 optimized local minima. Quantum mechanical calculations were carried out using the program Gaussian 03[61] for geometry optimizations, vibrational frequencies, and their intensities. The program GaussView[62] was used to visualize the vibrational displacements that form the basis of the vibrational mode descriptions given in Tables 3−5 and S1, S2, S4−S11, S13, S14).

Acknowledgment. This paper is dedicated to our friend and colleague, Professor Neil Bartlett, on the occasion of his 75th birthday and in recognition of his many outstanding contributions across a broad spectrum of fluorine chemistry. We thank the Natural Sciences and Engineering Research Council of Canada for support in the form of a research grant (G.J.S.) and the computational resources provided by SHARCNet (Shared Hierarchical Academic Research Computing Network; www.sharcnet.ca). We also thank Prof. Karl O. Christe (University of Southern California) for reading the manuscript and for providing helpful suggestions, and Dr. Jeremy C. P. Sanders for obtaining the initial ^{19}F and ^{129}Xe NMR spectra in CH_3CN solvent.

Supporting Information Available: Experimental Raman frequencies for $XeOF_2$, $F_2OXeN{\equiv}CCH_3$, $F_2OXeN{\equiv}CCH_3/CH_3CN/CH_3CN{\cdot}m$HF mixtures and $XeOF_2/F_2OXeN{\equiv}CCH_3$ mixtures (Table S1), CH_3CN (Table S2), and $CH_3CN{\cdot}m$HF (Table S3); calculated vibrational frequencies and geometries

(57) Sheldrick, G. M. *SADABS (Siemens Area Detector Absorption Corrections*), version 2.03; Madison, WI, 1999.
(58) Sheldrick, G. M. *SHELXTL-Plus*, release 5.1; Siemens Analytical X-ray Instruments, Inc.: Madison, WI, 1998.
(59) Spek, A. L. *J. Appl. Crystallogr.* **2003**, *36*, 7−13.
(60) Basis sets were obtained from the Extensible Computational Chemistry Environment Basis set Database, version 2/25/04, as developed and distributed by the Molecular Science Computing Facility, Environmental and Molecular Science Laboratory, which is part of the Pacific Northwest Laboratory, P.O. Box 999, Richland, WA 99352.
(61) Frisch, M. J.; et al. *Gaussian 98*, revision A.11; Gaussian, Inc.: Pittsburgh, PA, 2003.
(62) *GaussView*, release 3.0; Gaussian Inc.: Pittsburgh, PA, 2003.

for $XeOF_2 \cdot HF$ (Tables S4−S7), $XeOF_2 \cdot 2HF$ (Tables S8 and S9), $(XeOF_2)_2$ (Table S10), and $(XeOF_2)_3$ (Table S11); factor-group analysis for $F_2OXeN{\equiv}CCH_3$ (Table S12) and discussion; comparison of calculated and geometries for $XeOF_2$ using different levels of theory and basis sets (Table S13); calculated vibrational frequencies and geometries for XeF_4 (Table S14); calculated charges, bond orders, and valencies for the two experimental conformers of $F_2OXeN{\equiv}CCH_3$ (Table S15); calculated energies for all systems (Table S16); Cartesian coordinates for all systems (Table S17); the detailed synthesis of high-purity deuterium fluoride; complete reference 61; and the X-ray crystallographic file in CIF format for the structure determination of $F_2OXeN{\equiv}CCH_3$. This material is available free of charge via the Internet at http://pubs.acs.org.

JA0673480